



**HAL**  
open science

# Thermal and fluid flow modeling of the molten pool behavior during TIG welding by stream vorticity method

Abdel Halim Zitouni, Pierre Spiteri, Mouloud Aissani, Younes Benkheda

## ► To cite this version:

Abdel Halim Zitouni, Pierre Spiteri, Mouloud Aissani, Younes Benkheda. Thermal and fluid flow modeling of the molten pool behavior during TIG welding by stream vorticity method. *International Journal on Interactive Design and Manufacturing*, 2020, 14 (1), pp.173-188. 10.1007/s12008-020-00653-0 . hal-04594580

**HAL Id: hal-04594580**


**<https://ut3-toulouseinp.hal.science/hal-04594580v1>**

Submitted on 30 May 2024

**HAL** is a multi-disciplinary open access archive for the deposit and dissemination of scientific research documents, whether they are published or not. The documents may come from teaching and research institutions in France or abroad, or from public or private research centers.

L'archive ouverte pluridisciplinaire **HAL**, est destinée au dépôt et à la diffusion de documents scientifiques de niveau recherche, publiés ou non, émanant des établissements d'enseignement et de recherche français ou étrangers, des laboratoires publics ou privés.

# Thermal and fluid flow modeling of the molten pool behavior during TIG welding by stream vorticity method

Abdel Halim Zitouni<sup>1,3</sup>  · Pierre Spiteri<sup>2</sup> · Mouloud Aissani<sup>1</sup> · Younes Benkheda<sup>3</sup>

Received: 29 January 2019 / Accepted: 9 January 2020  
© Springer-Verlag France SAS, part of Springer Nature 2020

## Abstract

The present paper deals with the numerical simulation of weld pool development in Tungsten Inert Gas (TIG) process. A mathematical model is developed in order to solve the Navier–Stokes equations expressed in the stream–vorticity formulation coupled with heat equation taking into account the liquid solid phase change. Using the stream–vorticity formulation in incompressible fluid flow, the same problem is solved with reducing the number of transport equations. Therefore, only one transport equation (vorticity) and one Poisson equation (stream) are considered in this model. The FORTRAN programming and the numerical simulation are then achieved using appropriate discretization that ensures the convergence of the numerical methods to solve a large and sparse linear algebraic systems. Furthermore, to solve the radiation phenomena during welding described by the Stefan law, another method is proposed. The obtained numerical results are discussed and validated with experimental.

**Keywords** Thermal and fluid modeling · TIG welding · Stream vorticity · 304L steel · Numerical simulation

## 1 Introduction

The TIG welding is an assembly process by an electric arc. During welding, several physical phenomena occur, such as heat transfer, hydrodynamics, metallurgical transformation and electromagnetic phenomena; these ones have great effect on the microstructure and the morphology of the weld pool zone which affect the weld quality. Indeed, during the TIG welding, the weld pool is the location of a strong thermal gradient where temperature variation is very large; this variation ranges between the melting temperature of the metal on the edges of the weld pool and under the vaporization temperature of the metal in the center of the weld pool. This creates weldability problems such as: cracking solidification, appearance of porosity and the effect of residual stresses [1, 2] due to the occurrence of risk zones, denoted the fusion

zone (FZ) and the heat affected zone (HAZ), respectively. Lant et al. [1] indicated that the development of appropriate procedures is still an interest in weld repair, in order to extend the lifecycle of defective welded components beyond the temporary repair policies. Peng et al. [3] used a new image processing method to calculate and estimate the crack growth of an aluminum alloy weld. Therefore, through the development and improvement of technologies in order to solve welding problems, several tracks are followed; among them are predicted by mathematics and simulation.

Unfortunately, the mathematical models describing the physical phenomena are very hard to solve by an analytical way; consequently, it is the reason why numerical simulation have been used. Several research works as Varghese et al. [4] highlighted an increasing interest on numerical computation as a technique giving more knowledge and understanding of the welding processes and related the effects of the physical phenomena.

Thus, the simulation of the heat transfer and fluid flow in the weld pool has been the subject of various research works. In this work simulation results are compared with the ones presented below. Atthey [5] was one of the first to study the flow patterns in a hemispherical weld pool to determine the heat transfer during TIG welding process; by considering the electromagnetic force as the main

---

✉ Abdel Halim Zitouni  
halim0580@yahoo.fr

<sup>1</sup> Research Center in Industrial Technologies, CRTI, P.O. Box 64, 16014 Cheraga, Algiers, Algeria

<sup>2</sup> IRIT, INP-ENSEEIH, 2 Rue Charles Camichel, 31000 Toulouse, France

<sup>3</sup> Department of Mechanical Engineering, University of Blida 1, BP 270, Route de Soumaa, Blida, Algeria

entrainment force in the weld pool. Numerical simulation of welding of which objective the effect of fluid flow on the weld penetration considering three driving forces in the weld pool: the buoyancy, electromagnetic and surface tension has been the subject of various studies [6]. The use of a surface tension coefficient dependent on both the concentration of surfactant components (sulfur) and the temperature is introduced into a numerical study of TIG and laser welding by Zacharia et al. [7]; their purpose was to understand the heat flux and the influence of the flux of molten metal on the transient development of the weld pool. Goodarzi et al. [8] developed a 2D mathematical model for the weld pool in order to study the point angle effect of the electrode on the weld pool properties. Fan et al. [9] developed a numerical model to describe the weld pool partially or totally penetrated during TIG welding operation. The irregular shape of the weld pool and the solid liquid interface displacement are treated by boundary-fitted-coordinates technique. The physical domain represented by this system should be transformed into a rectangular domain before a standard finite difference method can be applied to solve the system. The complete models coupling the physics of the arc and weld pool were developed in two-dimensional axisymmetric TIG welding process [10–12]. In addition, a three-dimensional model of heat transfer and fluid flow to examine temperature profiles, velocity fields, the shape, the weld pool size and the solidified surface profile during gas metal arc fillet welding (GMAW) process was developed by Zhang et al. [13]. Recently Wang et al. [14] used an external magnetic field to control the flow and heat transfer in the melt to eliminate bump formation during GMAW welding. Kempf [15] offered an approximate analytical solution using a Green function approach to calculate the temperature field for a pulsed arc welding process. It described an explicit equation for temperature distribution, where only temporal integration must be resolved approximately. He compared these analytical results with that calculated by the finite elements method using the FEniCS computational code.

Interactivity is often associated with technologies that enable human–machine exchanges. The calculation and design steps are sometimes quite long. The aim of an interactive method is to best approach the preferences of the decision maker [16]: it is therefore in the interest of multiplying the exchange of information between the operational researcher and the decision-maker, i.e. shortening the steps of the procedure by limiting the calculations and the cost.

In an interactive approach, Madrid et al. [17]; propose the welding capability assessment method (WCAM) to identify and evaluate geometric design parameters that affect welding results, thereby compromising the quality and cost of product. The aim is to provide designers with a reliable database of welding capabilities when exploring and analyzing the design space of a number of product geometries.

The scope of this work is to provide a coupled model (heat equation and Navier–Stokes equation) leading to a numerical simulation in the design and geometry of the weld bead as well as the distribution of temperature during TIG welding of the 304L stainless steel sheet. The interactive approach consists of bringing back information about the welding parameters such as: welding current, gas flue, the heat input and the materials to be weld, introducing them into the virtual calculation code using Fortran program, in order to recover information about the temperature distribution, the field velocity in the weld pool, the size and the geometry of the weld bead and the HAZ. These given information can serve as database for the designers in the welding field.

The aim of the present study is to obtain a mathematical model using this formulation in order to predict the temperature and the velocity field in the weld pool during TIG welding. The mathematical model considered takes into account and combines the effect of the different driving forces in morphology and the size of the weld pool, particularly the surface tension force, the electromagnetic force and the natural convection force. Such model is obtained by coupling the heat equation with the Navier–Stokes equations. Due to the nonlinear formulation of these last equations, the stream–vorticity formulation of equations governing the fluid flow in the weld pool was developed and applied. Then, the diffusion equations coupled with convection–diffusion equations equipped with appropriate boundary conditions describing the physical process was solved. The nonlinearity being hard to be solved, the mathematical model developed to solve it is well described in this work. In order to carry out the numerical simulations, Fortran program is developed. In addition, Matlab software was used to display the graphical outputs. The results and discussions of numerical simulations are finally validated and presented; particularly the temperature profiles, velocity fields and the weld pool size.

## 2 Mathematical model

The schematic diagram of a cross section of the TIG welding process is shown in Fig. 1. The mathematical model describing the welding of the stainless steel 304L sheets is well described by the following coupled boundary values problems. The first equation describes the heat equation; the second equation describes the continuity equation and the behavior of the fluid is described by the Navier–Stokes equations. More precisely, the governing equations of heat transfer and fluid flow are coupled to the continuity equation taking into account the assumptions described below:

- two-dimensional symmetric heat transfer process with Oz being the axis of symmetry,

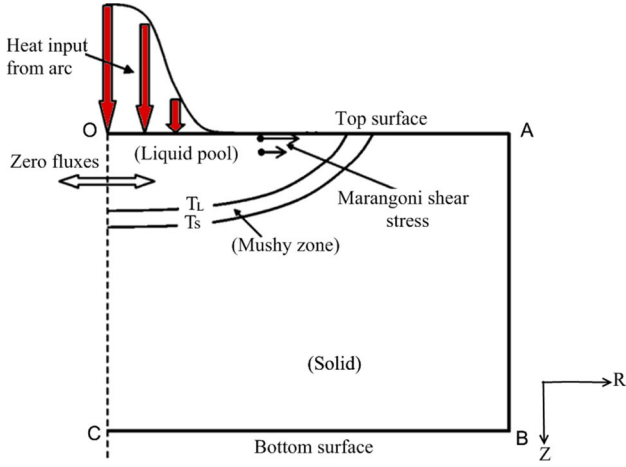


Fig. 1 Schematic diagram of welding cross section

- the physical properties are chosen to be constants, except the surface tension continuously dependent on the temperature,
- the sheet surface with no surface deformations,
- the liquid metal is an incompressible Newtonian fluid,
- the flow is laminar,
- the spatially-distributed heat and current fluxes falling on the free area have Gaussian characteristics,
- the Boussinesq approximation can be employed in our case in order to take into account the variation of density,
- approximate change of latent heat of melting for materials as linear.

Then the mathematical models are given below.

## 2.1 Heat equation

Taking into account the presence of a change in solid–liquid phase, the heat equation in cylindrical coordinates ( $r, z$ ) is expressed as:

$$\rho C_p \left( \frac{\partial T}{\partial t} + u \frac{\partial T}{\partial r} + w \frac{\partial T}{\partial z} \right) - k \frac{\partial^2 T}{\partial r^2} - k \frac{\partial^2 T}{\partial z^2} - \frac{k}{r} \frac{\partial T}{\partial r} = -\rho \Delta H \frac{\partial g_l}{\partial t} \quad (1)$$

where  $u$  and  $w$  are the velocity components,  $C_p$  is the specific heat capacity,  $k$  is the conductivity,  $\rho$  is the density,  $T$  is the temperature, and  $\Delta H$  is the latent heat of fusion.

Moreover the liquid fraction  $g_l$  is defined by

$$g_l = \begin{cases} 1 & T > T_L \\ \frac{T - T_S}{T_L - T_S} & T_S \leq T \leq T_L \\ 0 & T < T_S \end{cases} \quad (2)$$

where  $T_L$  and  $T_S$  respectively are the liquidus and solidus temperatures.

Because of the symmetry with respect to the centerline (weld) in this problem; our calculations were done only for one sheet (one side) to be weld as schemed in Fig. 1.

Because of the symmetry with respect to the centerline (weld) in this problem; our calculations were done only for one sheet (one side) to be weld as schemed in Fig. 1.

## 2.2 Continuity equation

The continuity equation is given by

$$\frac{u}{r} + \frac{\partial u}{\partial r} + \frac{\partial w}{\partial z} = 0 \quad (3)$$

## 2.3 Momentum equation

The radial expression of Navier–Stokes equation is presented as follows:

$$\rho \frac{\partial u}{\partial t} + \rho u \frac{\partial u}{\partial r} + \rho w \frac{\partial u}{\partial z} = -\frac{\partial p}{\partial r} + \mu \left( \frac{\partial^2 u}{\partial r^2} + \frac{1}{r} \frac{\partial u}{\partial r} - \frac{u}{r^2} + \frac{\partial^2 u}{\partial z^2} \right) + F_r \quad (4)$$

$$F_r = \left( \vec{J} \times \vec{B} \right)_r \quad (5)$$

The axial expression of Navier–Stokes equation is given by:

$$\rho \frac{\partial w}{\partial t} + \rho u \frac{\partial w}{\partial r} + \rho w \frac{\partial w}{\partial z} = -\frac{\partial p}{\partial z} + \mu \left( \frac{\partial^2 w}{\partial r^2} + \frac{1}{r} \frac{\partial w}{\partial r} + \frac{\partial^2 w}{\partial z^2} \right) + F_z \quad (6)$$

$$F_z = \left( \vec{J} \times \vec{B} \right)_z + \beta \rho g (T - T_0) \quad (7)$$

where  $p$  is the pressure,  $\mu$  is the dynamic viscosity,  $\beta$  is the coefficient of thermal expansion,  $g$  is the gravity,  $J$  is the welding current density,  $B$  is the magnetic induction,  $T_0$  is the reference temperature and in Eq. (4)  $F_r$  is the electromagnetic force in the radial  $R$  directions, and in (6)  $F_z$  is the sum of the buoyancy and electromagnetic forces in the axial  $Z$  direction given by (7).

## 3 Vorticity and stream formulation of the fluid flow equations

### 3.1 The transformed equations

In the present problem, the boundary value equations are defined in the two dimensional case. Moreover, the non-linearity in the corresponding model makes the resolution of the Navier–Stokes equations very difficult. Nevertheless consideration of only two dimensional case, the solution

of Navier–Stokes equations can be simplified when the vorticity and stream function formulation are used.

In such formulation the vorticity is defined by

$$\omega = \left( \frac{\partial u}{\partial z} - \frac{\partial w}{\partial r} \right) \quad (8)$$

Furthermore, the stream function  $\psi$  is expressed by

$$u = -\frac{1}{r} \frac{\partial \psi}{\partial z} \quad (9)$$

$$w = +\frac{1}{r} \frac{\partial \psi}{\partial r} \quad (10)$$

Using the vorticity and stream functions, the governing equations of fluid dynamic can be written easily

$$\begin{aligned} \frac{\partial \omega}{\partial t} + u \frac{\partial \omega}{\partial r} + w \frac{\partial \omega}{\partial z} - \frac{u\omega}{r} \\ = \nu \left( \frac{\partial^2 \omega}{\partial r^2} + \frac{1}{r} \frac{\partial \omega}{\partial r} + \frac{\partial^2 \omega}{\partial z^2} - \frac{\omega}{r^2} \right) \\ - \beta g \frac{\partial T}{\partial r} + \nabla \times (\vec{J} \times \vec{B}) \end{aligned} \quad (11)$$

$$-\omega = \frac{1}{r} \frac{\partial^2 \psi}{\partial z^2} + \frac{1}{r} \frac{\partial^2 \psi}{\partial r^2} - \frac{1}{r^2} \frac{\partial \psi}{\partial r} \quad (12)$$

In the Eq. (11) appears an electromagnetic force which can be computed by the solution of the Maxwell equations in coordinate system (r, z); this force is given by the following Eq. (13) [18].

$$\nabla \times (\vec{J} \times \vec{B}) = \frac{d\mu_0 I^2}{2\pi^2 e r^3} \left(1 - \frac{z}{e}\right) \left[1 - \exp\left(-\frac{r^2 d}{\sigma_j^2}\right)\right]^2 \quad (13)$$

where  $d$  is the length scale factor,  $I$  is the welding current,  $\mu_0$  is the magnetic permeability,  $\sigma_j$  is the current distribution parameter and  $e$  is the thickness of workpiece. The values of the physical coefficients are defined in Table 1.

## 3.2 Associated Boundary conditions

For the problem modeling of heat transfer and fluid flow behavior during TIG welding of stainless steel 304 L sheets, it is necessary to describe the boundary conditions in order to give a complete description of the phenomena.

### 3.2.1 Boundary conditions for the heat equation

On the borders of the work pieces the flux is imposed:

**Table 1** Physical coefficients of 304L stainless steel

Physical parameters	Symbol	Value	Unit
Specific heat capacity	$C_p$	602	J/(kg K)
Gravity acceleration	$g$	9.81	m/s <sup>2</sup>
Latent heat of fusion	$\Delta H$	272	kJ/kg
Coefficient of thermal expansion	$\beta$	10 <sup>-4</sup>	1/°K
Surface tension gradient	$\frac{\partial \gamma}{\partial T}$	-10 <sup>-4</sup>	N/(m K)
Liquidus temperature	$T_L$	1723	K
Solidus temperature	$T_S$	1673	K
Thermal conductivity of molten metal	$k_l$	20	W/(m K)
Thermal conductivity of solid metal	$k_s$	24	W/(m K)
Density of molten metal	$\rho_l$	6350	kg/m <sup>3</sup>
Density of solid metal	$\rho_s$	7500	kg/m <sup>3</sup>
Welding current	$I$	120	A
Welding arc voltage	$V$	14	V
Heat input efficiency	$\eta$	0.7	%
Magnetic permeability of vacuum	$\mu_0$	1.26 10 <sup>-6</sup>	H/m
Convective heat exchange coefficient	$h$	15	W/(m <sup>2</sup> K)
Stephan–Boltzman constant	$\sigma$	5.6710 <sup>-8</sup>	W/(m <sup>2</sup> K <sup>4</sup> )
Emissivity of body surface	$\epsilon$	0.82	-

- at the top surface OA, the heat source as Gaussian form [19] along  $R_0$  is applied.

$$-k \frac{\partial T}{\partial z} \Big|_{OA} = \frac{Q}{2\pi R_0^2} e^{-\left(\frac{3z^2}{R_0^2}\right)} \quad (14)$$

$$Q = \eta I V$$

where  $\eta$  is the heat input efficiency,  $I$  is the welding current,  $V$  is the welding arc voltage and  $R_0$  is the heat flux distribution radius parameter (m),

- on the right surface AB, there is an exchange by convection and radiation with ambient temperature,

$$-k \frac{\partial T}{\partial z} \Big|_{AB} = h(T - T_0) + \sigma_0 \epsilon (T^4 - T_0^4) \quad (15)$$

where  $\sigma_0$  is the Stefan-Boltzmann constant,  $\epsilon$  is the emissivity of body surface,

- on the bottom surface (BC), there is an exchange by adapted convection only (replaces conduction mode under sheet to be weld),

$$-k \frac{\partial T}{\partial r} \Big|_{BC} = h(T - T_0) \quad (16)$$

- A symmetry condition is on the OC surface.

$$\left. \frac{\partial T}{\partial r} \right|_{OC} = 0 \quad (17)$$

$$\omega|_{OC} = 0 \quad (19d)$$

### 3.2.2 Boundary conditions for the fluid equation

Starting from the classical momentum equation, the associated boundary conditions and their transformation according to the vorticity and stream formulation will be specified.

On the OA side of molten pool:

$$\begin{aligned} -\mu \left. \frac{\partial u}{\partial z} \right|_{OA} &= -\mu \left. \frac{\partial}{\partial z} \left( -\frac{1}{r} \frac{\partial \psi}{\partial z} \right) \right|_{OA} \Rightarrow \mu \left. \frac{1}{r} \frac{\partial^2 \psi}{\partial z^2} \right|_{OA} = \left. \frac{\partial \gamma}{\partial T} \frac{\partial T}{\partial r} \right|_{OA} \\ w|_{OA} &= \left. \frac{1}{r} \frac{\partial \psi}{\partial r} \right|_{OA} = 0 \Rightarrow \left. \frac{\partial \psi}{\partial r} \right|_{OA} = 0 \text{ and } \left. \frac{\partial^2 \psi}{\partial r^2} \right|_{OA} = 0 \\ -\omega|_{OA} &= \left. \frac{1}{r} \frac{\partial^2 \psi}{\partial z^2} \right|_{OA} \end{aligned} \quad (18a)$$

Then

$$\omega|_{OA} = -\frac{1}{\mu} \left. \frac{\partial \gamma}{\partial T} \frac{\partial T}{\partial r} \right|_{OA} \quad (18b)$$

where  $\gamma$  is the surface tension,

- on the BC and AB face there is no slip and the components of the velocity are zero

$$\begin{aligned} u|_{BC} = 0 &= \left. \frac{1}{r} \frac{\partial \psi}{\partial z} \right|_{BC} \Rightarrow \left. \frac{\partial \psi}{\partial z} \right|_{BC} = 0 \text{ and so } \left. \frac{\partial^2 \psi}{\partial z^2} \right|_{BC} = 0 \\ w|_{BC} = 0 &= \left. \frac{1}{r} \frac{\partial \psi}{\partial r} \right|_{BC} \Rightarrow \left. \frac{\partial \psi}{\partial r} \right|_{BC} = 0 \text{ and so } \left. \frac{\partial^2 \psi}{\partial r^2} \right|_{BC} = 0 \\ \omega|_{BC} &= 0 \end{aligned} \quad (19a)$$

$$\omega|_{AB} = 0 \quad (19b)$$

- on the OC face, no slip is assumed for the first component  $u$  of velocity; moreover for the second component  $w$ , the flux is zero. Then

$$\begin{aligned} u|_{OC} = 0 &= \left. \frac{1}{r} \frac{\partial \psi}{\partial z} \right|_{OC} \Rightarrow \left. \frac{\partial \psi}{\partial z} \right|_{OC} = 0 \text{ and so } \left. \frac{\partial^2 \psi}{\partial z^2} \right|_{OC} = 0 \\ \left. \frac{\partial w}{\partial r} \right|_{OC} = 0 &\Rightarrow \left. \frac{\partial}{\partial r} \left( \frac{1}{r} \frac{\partial \psi}{\partial r} \right) \right|_{OC} = 0 \Rightarrow \left. \frac{\partial w}{\partial r} \right|_{OC} = -\frac{1}{r^2} \left. \frac{\partial \psi}{\partial r} \right|_{OC} + \left. \frac{1}{r} \frac{\partial^2 \psi}{\partial r^2} \right|_{OC} = 0 \\ \omega|_{OC} &= -\left. \frac{1}{r} \frac{\partial^2 \psi}{\partial r^2} \right|_{OC} + \left. \frac{1}{r^2} \frac{\partial \psi}{\partial r} \right|_{OC} = 0 \end{aligned} \quad (19c)$$

## 4 Numerical solution

In the following, the coupled problem describing the welding of stainless steel 304L sheets is solved. Such problem consists in solving on the cross-section on one hand the Navier–Stokes equations formulated by the vorticity and stream function and on the other hand the heat equation. Taking into account the coupled equations, an analytical solution is very hard to obtain. Thus the Eqs. (1), (11) and (12) numerically will be resolved. For the numerical solution of the problem, a spatial discretization using the classical finite difference method is considered; the points are numbered from top to bottom and then from the left to the right according to the increasing abscissas. Therefore, the computational domain is divided into  $NZ + 1$  intervals along the OZ axis, each of interval length is  $h_z = \frac{L}{NZ+1}$  and into  $NR + 1$  intervals according to the R axis, each of length  $h_r = \frac{l}{NR+1}$  (Fig. 2).

The second derivative of the quantity  $\Theta$  with respect to  $r$  is approximated by

$$\frac{\partial^2 \Theta}{\partial r^2} \approx \frac{\Theta_{i+1} - 2\Theta_i + \Theta_{i-1}}{h_r^2} + O(h_r^2)$$

and accordingly for the second derivative with respect to  $z$ .

Moreover, for the first derivative of  $\Theta$  with respect to  $r$  a decentered scheme is considered and it is defined as:

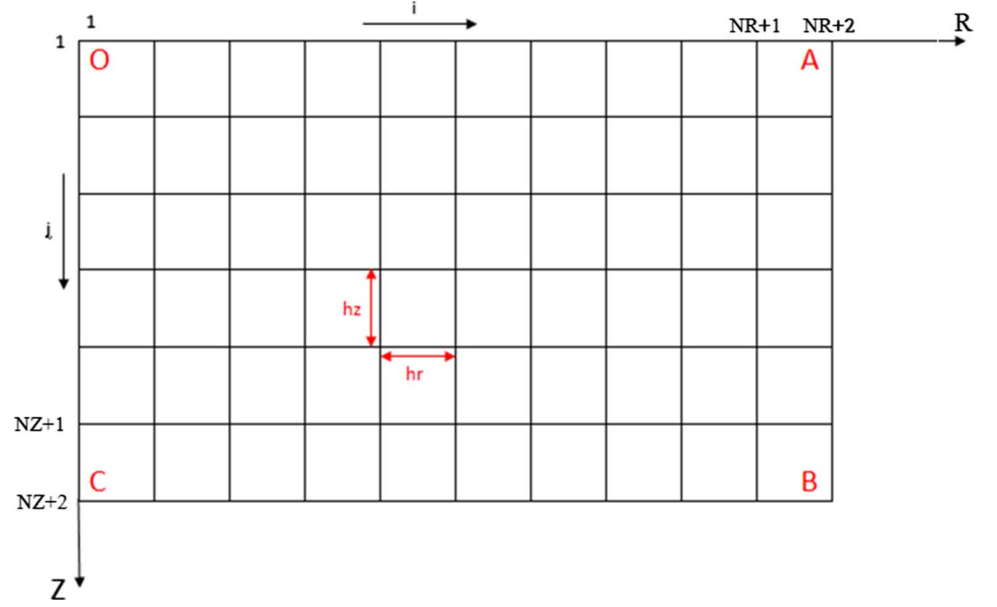
$$\alpha \frac{\partial \Theta}{\partial r} = \begin{cases} \alpha_i \frac{\Theta_i - \Theta_{i-1}}{h_r} + O(h_r) & \text{if } \alpha_i > 0 \\ \alpha_i \frac{\Theta_{i+1} - \Theta_i}{h_r} + O(h_r) & \text{if } \alpha_i < 0 \end{cases}$$

and accordingly for the first derivative with respect to  $z$ .

Such decentered scheme allows to obtain spatial diagonally dominant discretization matrices even more strictly diagonally dominant of the spatial part of the spatial discretization matrices.

For the temporal discretization, a preferably implicit time marching scheme is considered which is

**Fig. 2** Finite difference mesh of computed domain



unconditionally stable, while an explicit time marching scheme conditionally stable would involve to choose very small time step  $\Delta t$ . In this case combining the spatial and the temporal discretization lead to solve at each time step, the following nonlinear algebraic system where the mapping  $\Theta \rightarrow \Phi(\Theta)$  takes into account the convection and radiation phenomena on the boundary AB:

$$(\mathbf{Id} + \Delta t \mathbf{A}) \cdot \Theta^{n+1} + \Phi(\Theta^{n+1}) = \Delta t \cdot E^{n+1} + \Theta^n \quad (20)$$

where  $\mathbf{Id}$  is the identity matrix,  $\mathbf{A}$  is the spatial discretization matrix,  $E^{n+1}$  is the source term computed at step  $(n+1)$  and  $\Phi(\Theta^{n+1})$  represents the condition of convection-radiation given by

$$\Phi_j(T_j) = -k \frac{T_{j-1}^{n+1} - T_j^{n+1}}{h_z} - h(T_j^{n+1} - T_0) - \sigma_0 \epsilon \left( (T_j^{n+1})^4 - T_0^4 \right) \quad (21)$$

For the numerical solution of Eq. (20), it is necessary to consider a coupling of, on one hand, the Newton's method for the discretization points where the convection and radiation phenomena occur, and on the other hand, an iterative method (since the matrix  $\mathbf{A}$  is very sparse) for the other discretization points. The iterative method used in this work is the Gauss-Seidel method. Indeed, direct methods, like the Gauss method, are not very appropriate, due to the propagation of round-off errors which can produce wrong result. In such coupling of Newton's method with Gauss-Seidel method, the nonlinear equations and the linear equations are solved separately. Note that for the discretization points out of the boundary AB, the Gauss-Seidel method is well adapted to our case since the matrix  $\mathbf{A}$  is not symmetric. Moreover the Gauss-Seidel method converges whatever be

the initial guess of the solution since the matrix is strictly diagonal dominant.

For the discretization points belonging inside AB, NZ algebraic equations should be solved

$$\Phi_j(\theta_j) = 0, \quad j = 2, \dots, NZ + 1 \quad (22)$$

the Newton's method corresponds in fact to a local linearization of the mapping  $\theta_j \rightarrow \Phi_j(\theta_j)$  around an approximation of the solution; It is therefore necessary to implement for each component  $\theta_j$  the following iterative method

$$\theta_j^{q+1} = \theta_j^q - \frac{\Phi_j(\theta_j^q)}{\Phi_j'(\theta_j^q)} \quad j = 2, \dots, NZ + 1 \quad (23)$$

where  $q$  denotes the number of iteration of the Newton's method and the initial approximation  $\theta_j^0$  is given, for example, by the value obtained at the previous time step. Obviously, if the Newton's method converges, then the corresponding value obtained after convergence verify the exact Eq. (22). In order to briefly study the convergence of the Newton's method, let us denote by  $H(\theta)$  the right hand side of (23), then given by

$$H_j(\theta_j) = \theta_j - \frac{\Phi_j(\theta_j)}{\Phi_j'(\theta_j)}$$

Consider now the writing of the fixed point equation  $\theta_j = H_j(\theta_j)$ , for the exact solution  $\theta_j$  of (22) and also for a current iterate  $\theta_j^{q+1}$ ; by using the theorem of finite increments, the following simple calculation is obtained:



$$|\theta_j - \theta_j^{q+1}| \leq L |\theta_j - \theta_j^q| \leq \dots \leq L^{q+1} |\theta_j - \theta_j^0|$$

where  $L = \text{Sup}_{\tau \in I} |H'(\tau)|$  where  $I$  is the interval on which  $H'$  is defined; then the Newton's method converges if  $L < 1$ . Note that for the exact  $\theta_j$  value:

$$H'_j(\theta_j) = \frac{\Phi_j(\theta_j)\Phi_j''(\theta_j)}{(\Phi_j'(\theta_j))^2} = 0.$$

Since (22) is verified.

Then, since  $H'_j(\theta_j)$  is continuous, there exists a closed interval around the exact value  $\theta_j$  where  $L < 1$  and the Newton's method is locally convergent. Concerning the asymptotic convergence rate, considering the Taylor's development limited to order two of  $(\theta_j - \theta_j^{q+1})$ , we obtain in a straightforward way

$$\theta_j - \theta_j^{q+1} = \frac{(\theta_j - \theta_j^q)^2}{2!} H''(\tilde{\theta}_j), \quad \theta_j < \tilde{\theta}_j < \theta_j^q$$

Since  $H'_j(\theta_j) = 0$ ; the convergence of the Newton's method is quadratic and the implementation of such iterative method is very efficient for the solution of (22).

In the present work, a regular distribution of nodes in the radial direction in conjunction with uniform distribution in the Z direction is used. The domain is meshed by  $100 * 50$  cells. The convergence criterion was set at a maximum relative error for all dependent variables ( $\psi$ ,  $\omega$ , T) to be less than  $10^{-6}$  and corresponds to the satisfaction of the following inequality (23):

$$\frac{\sum_{i=1}^{NR+2} \sum_{j=1}^{NZ+2} |\Theta_{ij}^{new} - \Theta_{ij}^{old}|}{\Theta_{max}} \leq \epsilon \quad (24)$$

where  $\Theta^{new}$  is the updated value of  $\Theta$  and  $\Theta^{old}$  is the previous value of  $\Theta$ .

Then all remaining variables as  $u$ ,  $w$ ,  $g_1$  ...etc. can be deduced.

## 5 Results and discussion

The numerical model of heat transfer coupled with the one describing the fluid flow is used to compute the temperature fields, the velocity fields, the liquid fraction, the weld pool size and the morphology (FZ) as well as the size of the heat-affected zone (HAZ) during a TIG welding operation of stainless steel 304 L sheets. The weld is performed in a butt joint configuration without a filler metal in case of a negative

surface tension gradient  $\frac{\partial \gamma}{\partial T} < 0$ . The welding characteristics used for the calculations are given in Table 1.

Figure 3a, b represent the predicted temperature in the weld pool and in the base metal at both instants  $t=1$  s and  $t=2$  s as well as the maximum temperature located at the top corresponding to the point O of Fig. 2. This maximum value is about 2000 K; it is greater than the melting temperature of 304L stainless steel which equals 1723 K. It can be observed that the temperatures vary in regard to the time with the maximum value of the order of 2800 K reached at  $t=2$  s. This value is considerably greater than the melting temperature of this stainless steel. The evolution over time of the temperature distribution during the welding process leads to the appearance of a moved liquid zone under heat source whose size increases; it can be seen also the cooling rates towards the edges of the sheet to be welded, this induces a change in their microstructure [20].

The isothermal curves and the fraction of liquid calculated at instants 2 s are shown in Figs. 4 and 5 respectively. The isothermal curves are very close to one another at the point of maximum temperature and more disperse by moving away from this point. The different zones corresponding to different states of the material are predicted by the values of the isothermal curves, in particular the liquid zone (ZF) and the heat affected zone (HAZ) (see Fig. 4); The liquid zone ZF is delimited by the isotherms which give the maximum temperature and the melting temperature of 1723 K; on the other hand, the zone HAZ is delimited also by the isotherms of the melting temperature and those give the eutectoid temperature set at 996 K [20].

Recall that the eutectoid temperature is a characteristic temperature indicating the starting of variations in microstructure which occur due to the change in solubility of the various species in the steel. According to the Iron-Carbon phase diagram, the eutectoid temperature is used as a criterion to determine the transition between the base metal and the zone affected by heat [20].

At  $t=2$  s, the size of the weld pool increased to have a depth of  $Lp=1.7$  mm and a width of  $Lw=6.6$  mm (see Fig. 5), so in this case the ratio is  $\frac{Lp}{Lw} = 0.26$ . These results obtained by our methodology and technique are in good agreement with those found in the Ref. [21, 22]. In this period the heat affected area (HAZ) increased also considerably to a depth of 3 mm, and a width of 3.40 mm on the upper side and 7.67 mm on the underside of the sheet.

Figure 6 represents the velocity fields in liquid metal region due to the surface tension force exerted on the weld pool surface. To give a clear explanation of these results, it is recalled that the surface tension of the molten metal increases as it moves away from the center of the weld pool, that is to say for the higher temperatures, it gives a negative surface tension gradient.



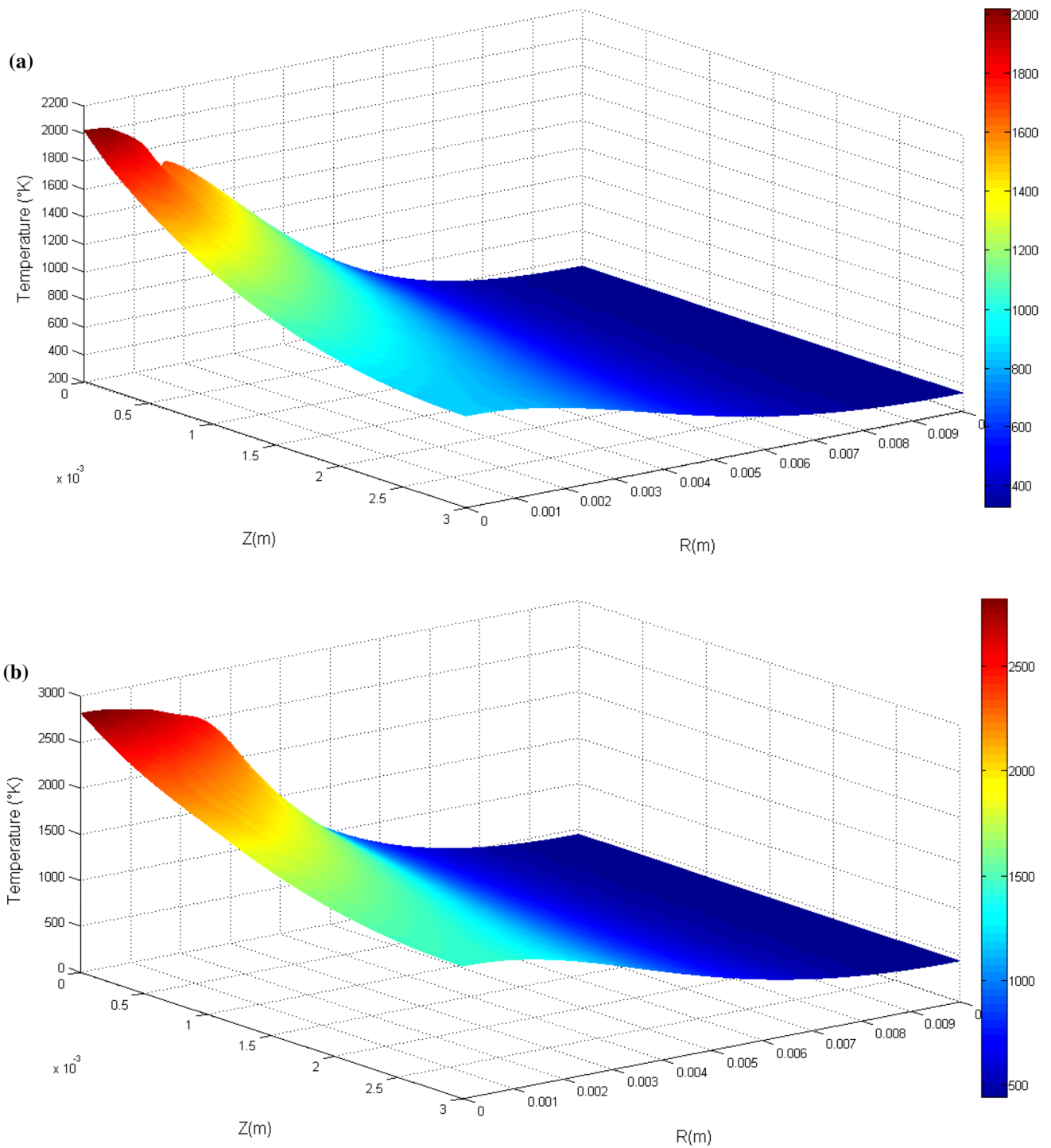


**Fig. 3** a Temperature field distribution  $t = 1$  s. b Temperature field distribution  $t = 2$  s

In the case of a negative gradient, the velocity vectors at the surface of the weld pool are directed towards the outside and the flow at the surface of the weld pool is radial and also directed towards the outside, which gives a centrifugal stirring [22, 23].

The penetration of the weld pool and its width are respectively  $L_p = 1.0$  mm and  $L_w = 6.6$  mm, so the ratio  $\frac{L_p}{L_w} = 0.15$  which gives a wetting weld pool, thereby confirming that the surface tension force preclude the penetration of weld pool when the surface tension gradient is

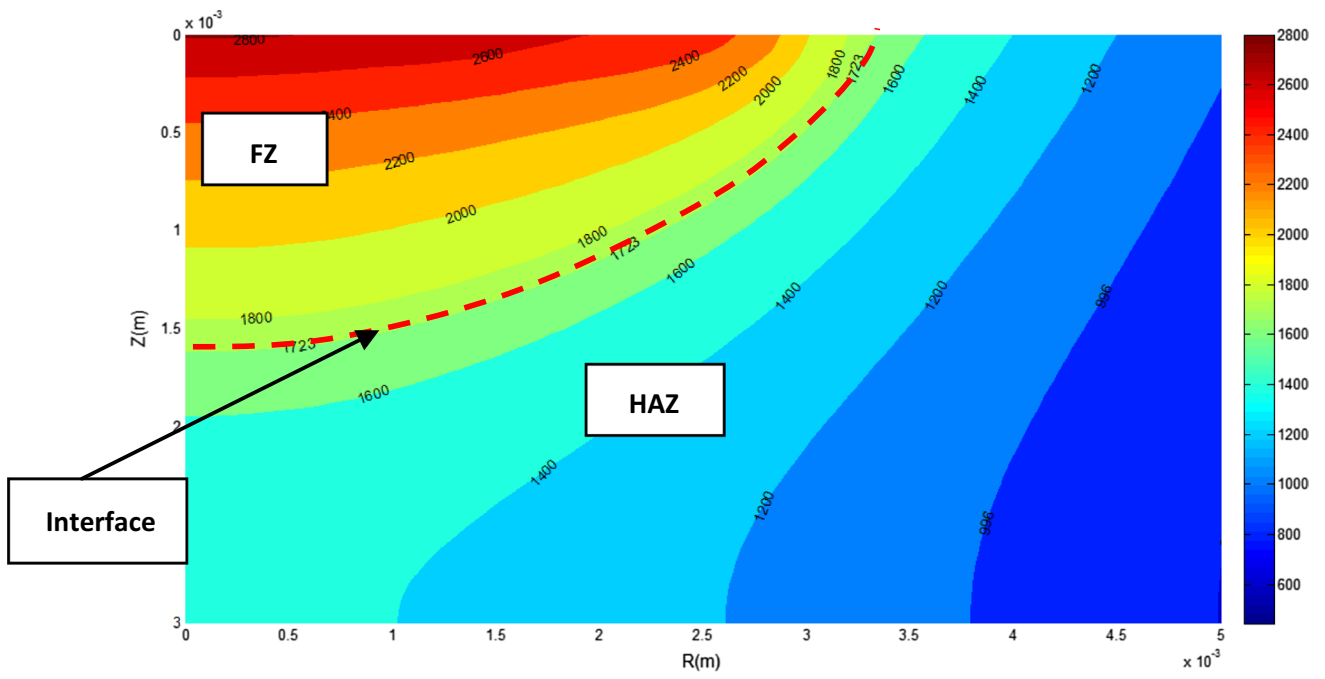


Fig. 4 Isotherm curves calculated  $t = 2$  s

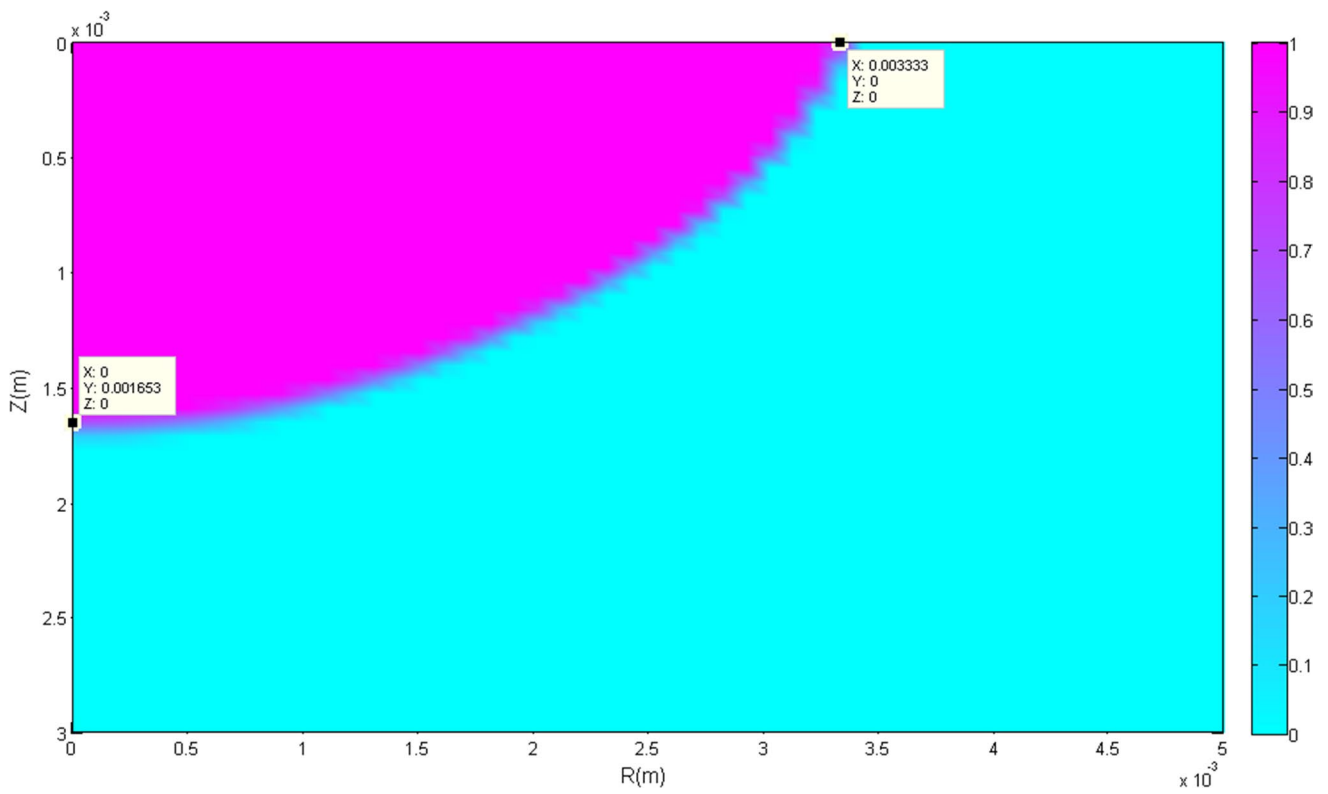
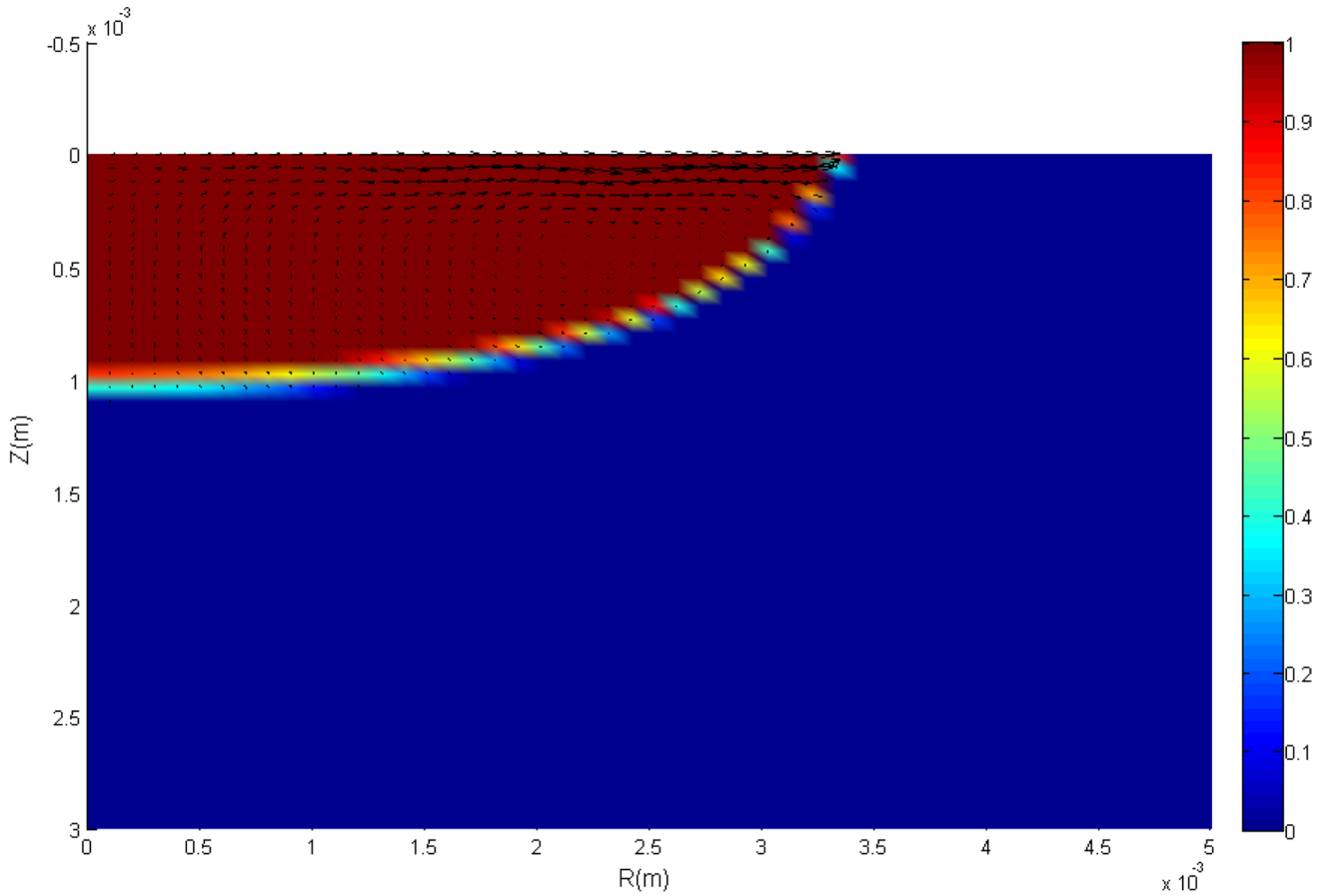


Fig. 5 Fraction of liquid calculated  $t = 2$  s



**Fig. 6** Orientation of the velocity field calculated at  $t=2$  s induced by the surface tension force

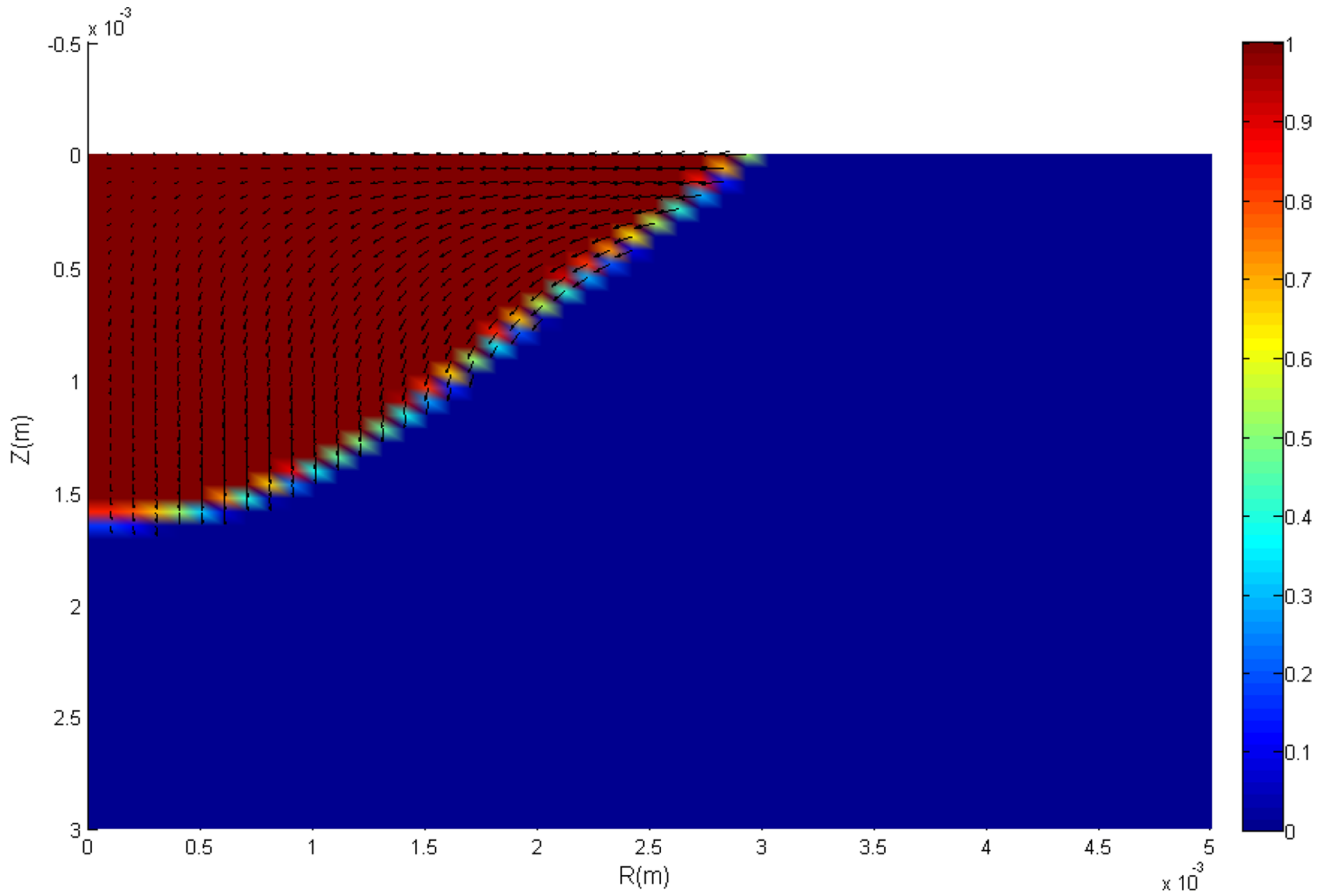
negative. Note that the maximum velocities reached in the weld pool have a value of about 8.5 cm/s.

Figure 7 represent the fluid velocity field calculated at  $t=2$  s; the effects observed are due to the action of an electromagnetic force only caused by the interaction between the electric current passing through the weld pool and the magnetic field which it generates. The velocity vectors are directed inwards and downwards from the top center of the weld pool. Moreover the flow of the fluid on the surface of the weld pool is radial and directed inwards which causes a centripetal stirring. The penetration of the weld pool is about  $L_p = 1.6$  mm and its width  $L_w$  is 5.8 mm; thus, so the ratio  $\frac{L_p}{L_w} = 0.28$ , is increased by about 60% compared to penetration calculated only with the surface tension force, confirming that the electromagnetic force favors the penetration of the weld pool and has inverse effects compared to those caused by the surface tension force. In that case, the maximum velocity in the weld pool is 2.5 cm/s.

The velocity field due to the natural convection force is illustrated in Fig. 8. This natural convection force, also called the buoyancy force, is derived from the effect of density in the molten zone. Indeed, the density of the metal in

the liquid phase depends on the temperature and varies in the molten material volume. The velocity vectors are oriented towards the outside of the weld pool and from bottom to top; the flow in the weld pool surface is directed outwardly from there. The penetration of the weld pool due to the natural convection force is approximately  $L_p = 1.16$  mm, its width being  $L_w = 5.60$  mm. The natural convection force thus favors a wetting weld pool which gives a weak centrifugal stirring in comparison with the two latter forces. The maximum speed due to the natural convection force is of the order of 0.2 cm/s; this value is very low with respect to the speed due to the surface tension force and the electromagnetic force. The results regarding the velocity fields calculated by our model are in good agreement with the literature [24].

Figure 9 shows the shape and the size of the weld pool without taking into account the convective effect, so only conduction effect is taken into account. The penetration and the width of the weld pool calculated with the conduction model gives approximately the following values  $L_p = 1.16$  mm and  $L_w = 5.60$  mm. It should be noted that the size of the weld pool is identical to that obtained when the natural convection force is taken into account; so this



**Fig. 7** Orientation of the velocity field calculated at  $t=2$  s induced by the electromagnetic force

confirms that the natural convection force is small and that it has no great effect on the morphology and on the size of the weld pool.

Figures 10 and 11 represent the field and the magnitude of the fluid velocities induced by the resultant of the three driving forces taken into account by our model such that the surface tension gradient is negative. Note that the three forces taken into account here are the surface tension force, the electromagnetic force and the natural convective force. The velocity vectors are oriented outwardly from the center, so the flow at the weld pool surface transports the energy delivered by the heat source to the outside, which results in high centrifugal stirring. The penetration and the weld pool width are respectively  $L_p = 1.6$  mm and  $L_w = 6.6$  mm with a ratio of  $\frac{L_p}{L_w} = 0.24$ . The fluid has a maximum velocity on the upper side away from the center of the heat source; the corresponding value of the velocity is about 11 cm/s [12], which shows that the surface tension force dominates the driving forces in the weld pool; thus, when the surface tension gradient is negative, there will be a wetting weld pool [23, 25]. It can be seen in Fig. 11 that the velocity magnitude

has a wave shape, due to the fact that each driving force acts differently on the weld pool.

When the surface tension gradient is negative, Fig. 12 shows the profiles of the radial velocities on the upper face of the weld pool calculated by our model at  $t=2$  s taking into account each driving force alone and the resultant of the three forces: the surface tension force, the electromagnetic force and the natural convection force. It can be noted that there is a notable difference between the calculated maximum velocities taking into account the different driving forces in the weld pool and those maximum velocities are located near the edges of the weld pool favoring the stirring process and heat conduction toward solid regions. Furthermore, the Marangoni effect dominates the driving forces on the upper surface of the weld pool. However the Buoyancy force has the weakest effect due to its nature. Figure 13 shows the evolution of the penetration and the half width of the weld pool as well as the ratio (penetration over the half width)  $\frac{L_p}{0.5L_w}$  calculated by our model, taking into account the resultant of all driving forces in the weld pool as a function of time. Penetration and half-width increase as a function of

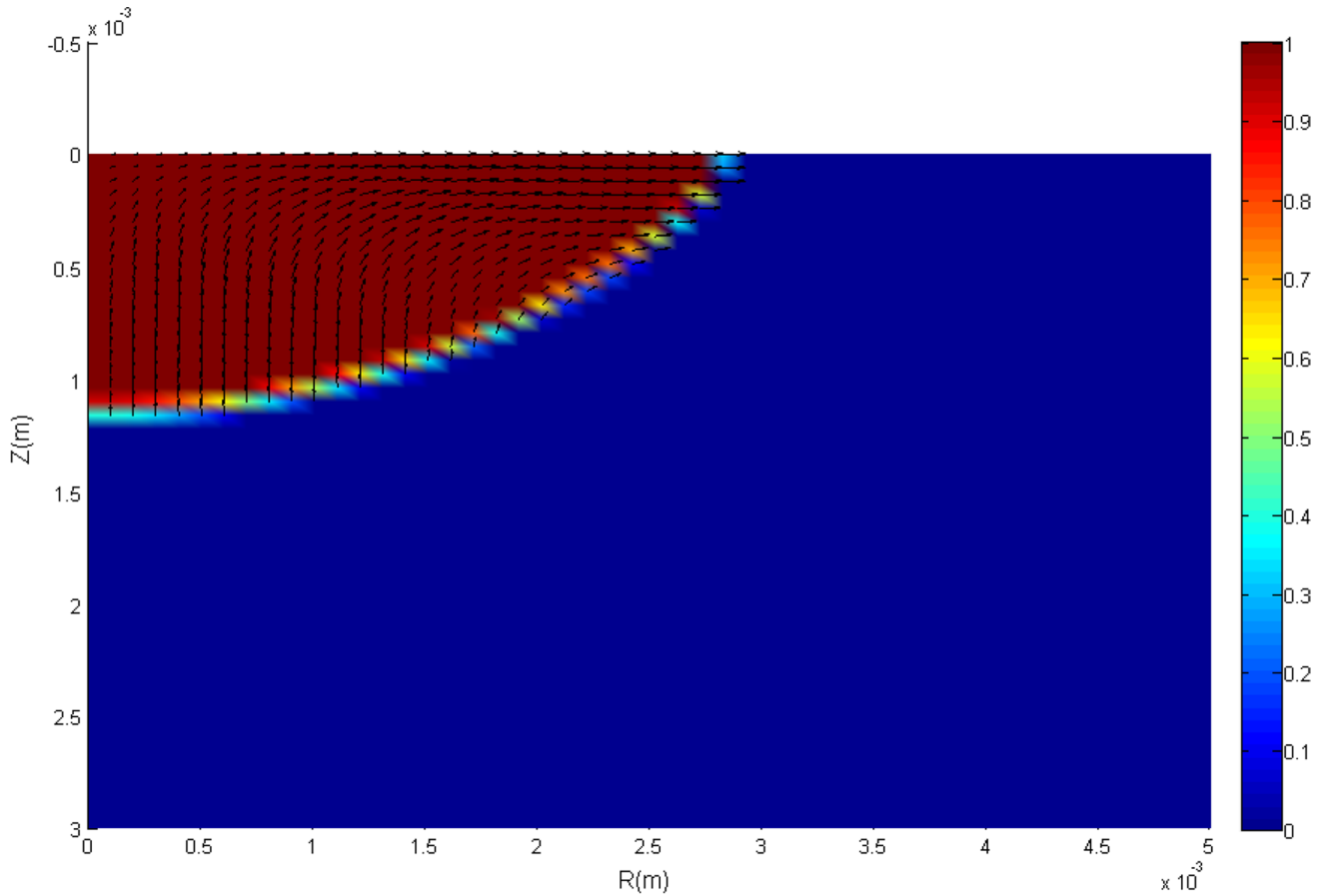


Fig. 8 Orientation of the velocity fields computed at  $t=2$  s induced by the convection force

time; such that the half width increases faster than penetration, reaching a value of 3.4 mm at  $t=2$  s.

The ratio  $\frac{L_p}{0.5L_w}$  increases between the initial time and  $t=1.4$  s, then this ratio remains practically constant to reach an asymptotic value  $\frac{L_p}{0.5L_w} = 0.5$  at  $t=2$  s, giving a wetting weld pool. These results are in good agreement with the experimental results presented in [22].

The evolution of the radial temperature on the upper face for each driving force in the weld pool and for the resultant of forces is shown in Fig. 14. The radial temperature profile on the surface of the weld pool calculated taking into account the natural convection force is similar to that calculated by the conduction model; these profiles have a Gaussian distribution with a maximum value of about 2580 K. This confirms that the natural convection force has no influence on the profile and the calculated maximum temperature. The maximum temperature calculated by the model taking into account the electromagnetic force has increased to a value of about 2800 K; on the other hand the temperature has kept the same profile as that calculated by the model with conduction alone.

The temperature profile calculated taking into account the surface tension force with a negative gradient is different from that calculated using the model with conduction alone in the part where there is the metal in the liquid phase. The maximum temperature in this case is about 2400 K; it slowly decreases on the upper side of the weld pool to the liquid–solid transition zone or it will decrease rapidly. In the solid part the temperature follows the shape of the Gaussian calculated by the model with conduction alone. The temperature profile calculated with the result of the driving forces has practically the same shape as that calculated with the model taking into account the surface tension force only with a maximum temperature increase which is of the order of 2800 K. This result confirms that the surface tension has a major effect on the temperature profile calculated by our model. These results are in good agreement with the literature [22].

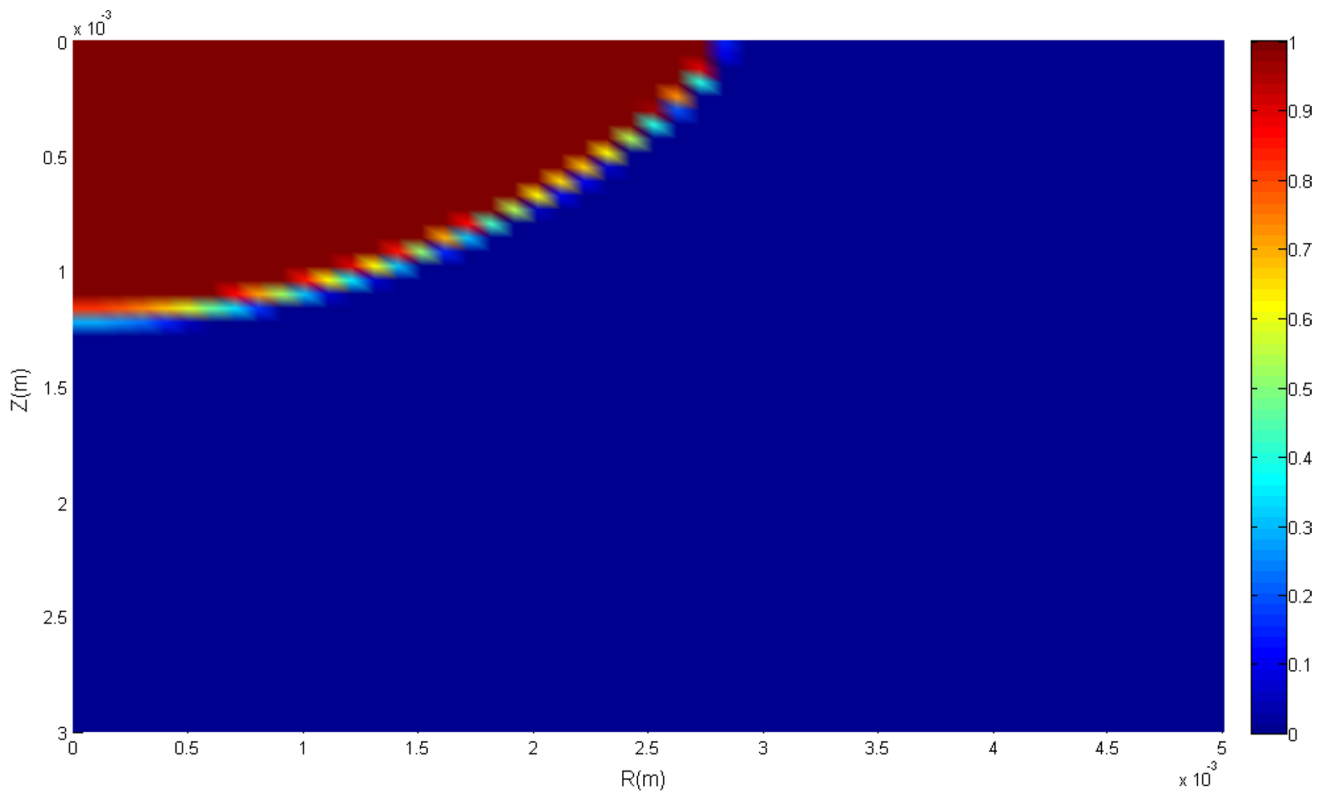


Fig. 9 Fraction of the liquid calculated at  $t = 2$  s in conduction alone

## 6 Conclusion

In this work, a FORTRAN code was developed to carry out the numerical resolution of sparse algebraic systems arising from discretization by the finite difference method of the heat equation coupled with the Navier–Stokes equations expressed in the stream–vorticity formulation. This model was used to simulate the TIG welding of the 304L Stainless steel sheet.

The following conclusions can be drawn:

- The mathematical model developed in order to solve the heat equation coupled with the Navier–Stokes equations expressed in the stream–vorticity formulation permits to simplify the formulation of the Navier–Stokes equations by the elimination of the mass conservation equation and the pressure field.
- The temporal evolution of the temperature distribution during the welding process results in a widening of the liquid zone at  $t = 2$  s with a maximum temperature of 2800 K.
- The penetration and the half-width of the weld pool (1.6 mm, 3.4 mm, respectively) calculated from the isotherms at  $t = 2$  s are in good agreement with the literature.
- The field and the magnitude of the velocities calculated taking into account the three driving forces taken individually, the surface tension force, the electromagnetic force and the natural convection force, show a good agreement with the literature.
- The field and magnitude of the velocities due to the resultant of the three driving forces when the surface tension gradient is negative show that the surface tension force dominates the driving forces in the weld pool and favors a weld pool wetting.
- The evolution of the radial temperature at the upper surface for each driving force in the weld pool and for the resultant forces confirms that the surface tension has a major effect on the calculated temperature profile.
- The numerical simulation results obtained by our FORTRAN code can be used as a database of the weld bead geometry and its formation conditions (i.e.: thermal behavior and fluid mechanics) as a function of the welding process parameters. Furthermore, it allows designers to create an interactive engineering platform that can be used as a decision support tool for the benefit of the design engineers through, for instance, TIG weld bead.



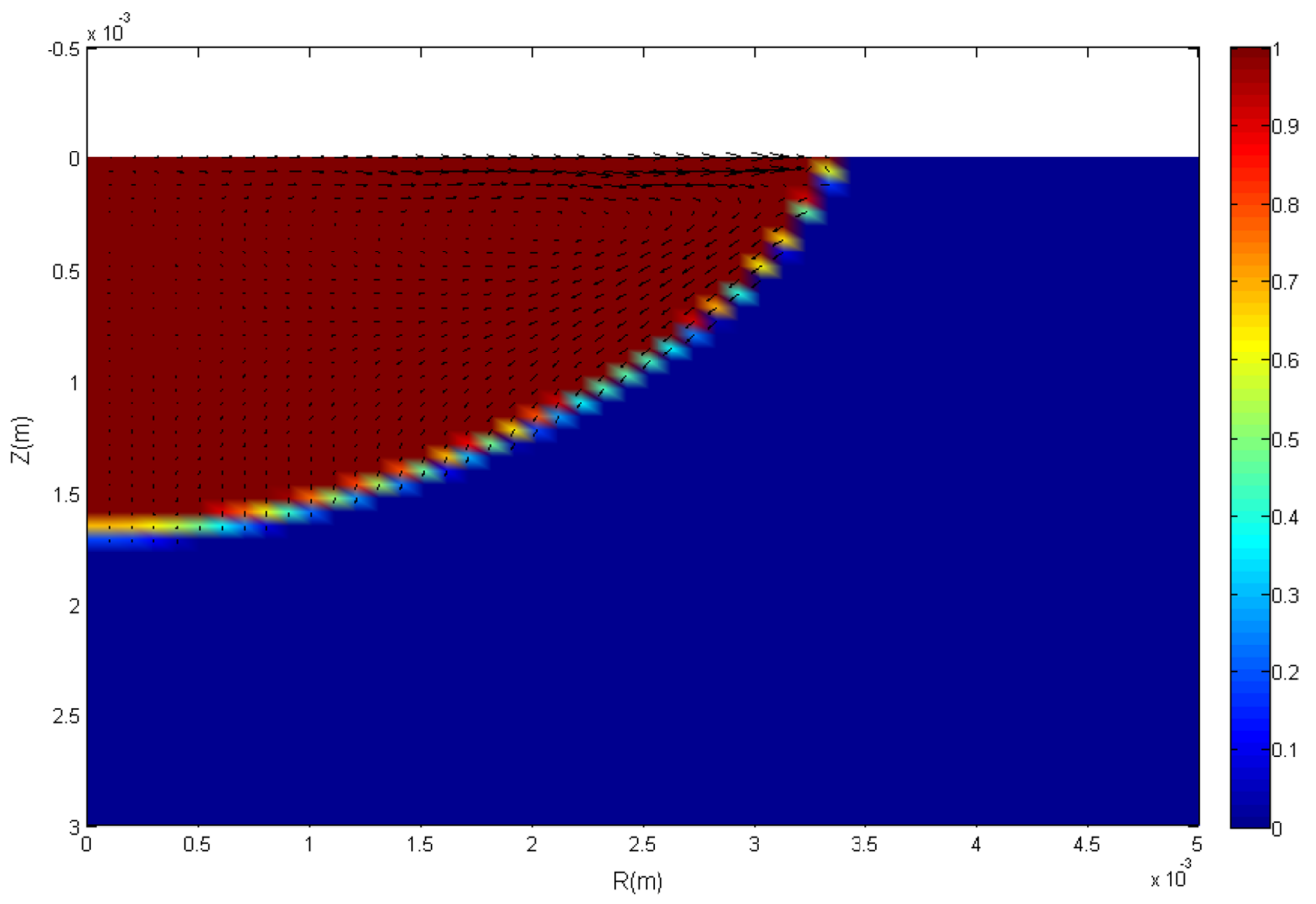


**Fig. 10** Orientation of the velocity fields calculated at  $t=2$  s induced by the resultant of the forces

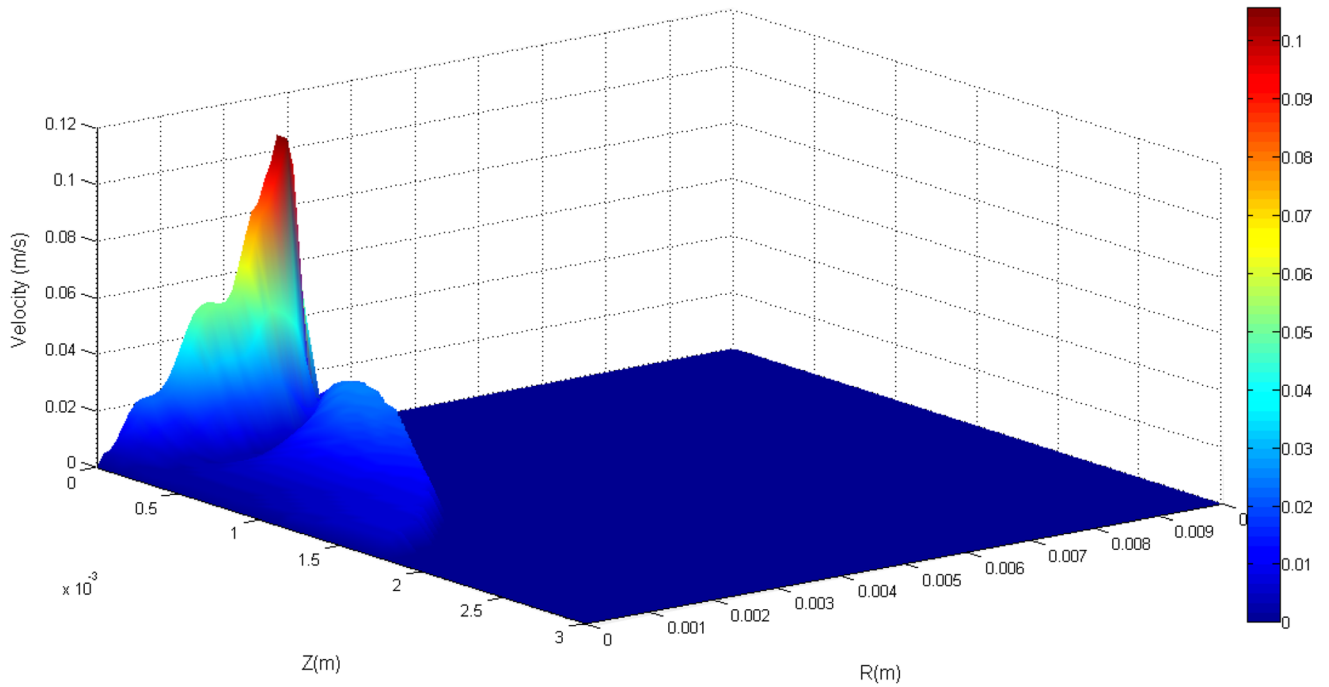


**Fig. 11** Magnitude of the velocity fields calculated at  $t=2$  s induced by the resultant of forces

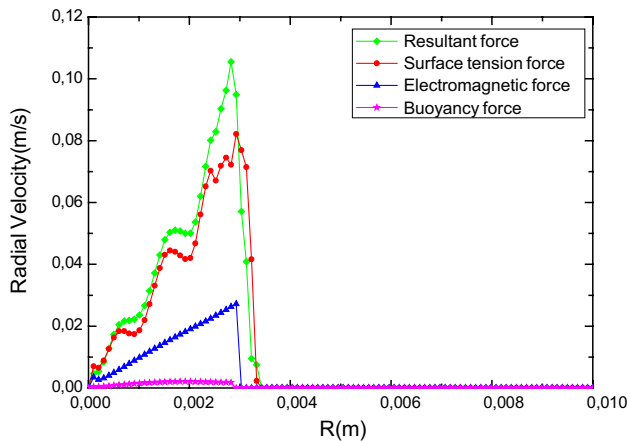


Fig. 12 Radial fluid velocity on the top surface as a function of radial position

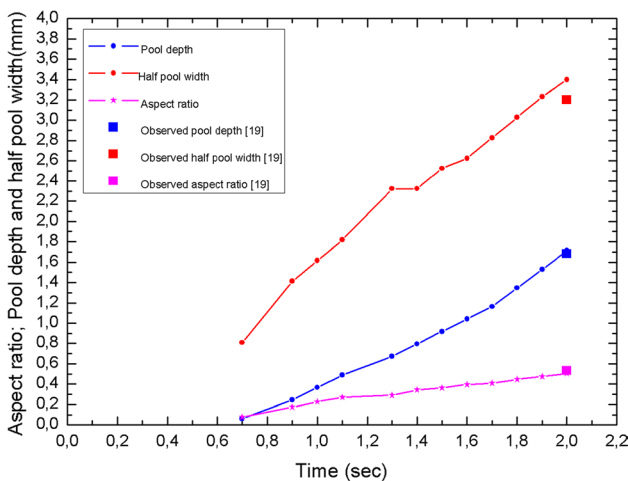


Fig. 13 Computed weld pool depth, half width and aspect ratio

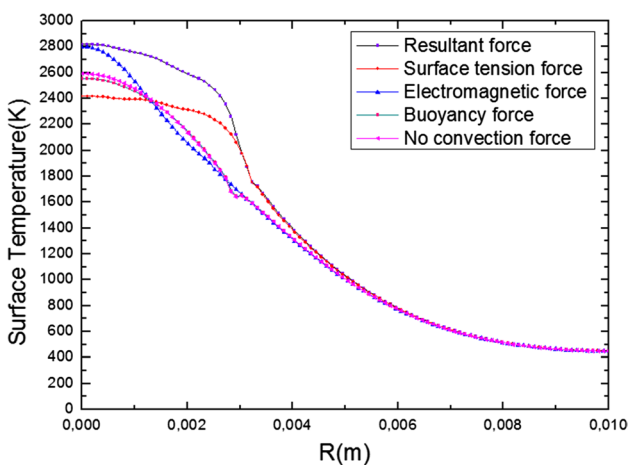


Fig. 14 Upper surface temperature as a function of radial position

## References

- Lant, T., Robinson, D.L., Spafford, B., Storesund, J.: Review of weld repair procedures for low alloy steels designed to minimise the risk of future cracking. *Int. J. Press. Vessels Pip.* **78**, 813–818 (2001)
- Lucjan, W.: Failure analysis of the wing-fuselage connector of an agricultural aircraft. *Eng. Fail. Anal.* **13**(4), 572–581 (2006)
- Peng, Q.H., Liu, T., Sun, Q.: Reliability estimation for aluminum alloy welded joint with automatic image measurement of surface crack growth. *Eng. Comput.* **33**(4), 1205–1223 (2016)
- Varghese, V.M.J., Suresh, M.R., Kumar, D.S.: Recent developments in modeling of heat transfer during TIG welding—a review. *Int. J. Adv. Manuf. Technol.* **64**(5), 749–754 (2013)
- Atthey, D.R.: A mathematical model for fluid flow in a weld pool at high currents. *J. Fluid Mech.* **98**(4), 787–801 (1980)
- Kou, S., Wang, Y.H.: Computer simulation of convection in moving arc weld pools. *Metall. Trans. A* **17**(12), 2271–2277 (1986)
- Zacharia, T., David, S.A., Vitek, J.M., Debroy, T.: Weld pool development during GTA and laser beam welding of type 304 stainless steel, part I—theoretical analysis. *Weld. J* **68**(12), 499–509 (1989)
- Goodarzi, M., Choo, R., Takasu, T., Toguri, J.M.: The effect of the cathode tip angle on the gas tungsten arc welding arc and weld pool: II. The mathematical model for the weld pool. *J. Phys. D Appl. Phys.* **31**(5), 569–583 (1999)
- Fan, H.G., Tsai, H.L., Na, S.J.: Heat transfer and fluid flow in a partially or fully penetrated weld pool in gas tungsten arc welding. *Int. J. Heat Mass Transf.* **44**(2), 417–428 (2001)
- Tanaka, M., Terasaki, H., Ushio, M., Lowke, J.J.: A unified numerical modeling of stationary tungsten-inert-gas welding process. *Metall. Mater. Trans. A* **33**(July), 2043–2052 (2002)
- Traidia, A., Roger, F.: Numerical and experimental study of arc and weld pool behaviour for pulsed current GTA welding. *Int. J. Heat Mass Transf.* **54**(9–10), 2163–2179 (2011)
- Wang, X., Huang, J., Huang, Y., Fan, D., Guo, Y.: Investigation of heat transfer and fluid flow in activating TIG welding by numerical modeling. *Appl. Therm. Eng.* **113**, 27–35 (2017)
- Zhang, W., Kim, C.-H., DebRoy, T.: Heat and fluid flow in complex joints during gas metal arc welding—part I: numerical model of fillet welding. *J. Appl. Phys.* **95**(9), 5210 (2004)
- Wang, L., Wu, C., Chen, J., Gao, J.: Influence of the external magnetic field on fluid flow, temperature profile and humping bead in high speed gas metal arc welding. *Int. J. Heat Mass Transf.* **116**, 1282–1291 (2018)
- Kempf, V.: Approximated analytical approach for temperature calculation in pulsed arc welding. *Int. J. Interact. Des. Manuf.* (2019). <https://doi.org/10.1007/s12008-019-00638-8>
- Fischer, X., Nadeau, J.-P.: Interactive design: then and now. In: *Research in Interactive Design*, vol. 3, pp. 1–5. Springer, Paris (2011)
- Madrid, J., Forslund, A., Söderberg, R., et al.: A welding capability assessment method (WCAM) to support multidisciplinary design of aircraft structures. *Int. J. Interact. Des. Manuf.* **12**, 833–851 (2018)
- Kumar, A., DebRoy, T.: Calculation of three-dimensional electromagnetic force field during arc welding. *J. Appl. Phys.* **94**(2), 1267–1277 (2003)
- Goldak, J., Chakravarti, A., Bibby, M.: New finite element model for welding heat sources. *Metall. Trans. B Process. Metall.* **15**(2), 299–305 (1984)
- Aissani, M., Guessasma, S., Zitouni, A., Hamzaoui, R., Bassir, D., Benkedda, Y.: Three-dimensional simulation of 304L steel TIG welding process: contribution of the thermal flux. *Appl. Therm. Eng.* **89**, 822–832 (2015)

21. Trautmann, M., Hertel, M., Füssel, U.: Numerical simulation of TIG weld pool dynamics using smoothed particle hydrodynamics. *Int. J. Heat Mass Transf.* **115**, 842–853 (2017)
22. Kim, W.H., Fan, H.G., Na, S.J.: Effect of various driving forces on heat and mass transfer in arc welding. *Numer. Heat Transf. Part A Appl.* **32**(6), 633–652 (1997)
23. Zhang, W., Roy, G.G., Elmer, J.W., DebRoy, T.: Modeling of heat transfer and fluid flow during gas tungsten arc spot welding of low carbon steel. *J. Appl. Phys.* **93**(5), 3022–3033 (2003)
24. Li, Y., Feng, Y., Li, Y., Zhang, X., Wu, C.: Plasma arc and weld pool coupled modeling of transport phenomena in keyhole welding. *Int. J. Heat Mass Transf.* **92**, 628–638 (2016)
25. Berthier, A., Paillard, P., Carin, P.M., Valensi, F., Pellerin, S.: TIG and A-TIG welding experimental investigations and comparison to simulation. *Sci. Technol. Weld. Join.* **17**(8), 609–615 (2012)

**Publisher's Note** Springer Nature remains neutral with regard to jurisdictional claims in published maps and institutional affiliations.